

# Transmural wave speed gradient may distinguish intrinsic myocardial stiffening from preload-induced changes in operational stiffness in shear wave elastography

Annette Caenen\*, *Member, IEEE*, Stéphanie Bézy, Aniela Petrescu, Annegret Werner, Jens-Uwe Voigt, Jan D'hooge<sup>#</sup>, *Senior Member, IEEE*, and Patrick Segers<sup>#</sup>, *Senior Member, IEEE*

**Abstract—** *Background:* Shear wave elastography (SWE) is a promising technique to non-invasively assess myocardial stiffness based on the propagation speed of mechanical waves. However, a high wave propagation speed can either be attributed to an elevated intrinsic myocardial stiffness or to a preload-induced increase in operational stiffness. *Objective:* Our objective was to find a way to discriminate intrinsic myocardial stiffening from stiffening caused by an increased pressure in SWE. *Methods:* We used the finite element method to study the shear wave propagation patterns when stiffness and/or pressure is elevated, compared to normal stiffness and pressure. Numerical findings were verified in a few human subjects. *Results:* The transmural wave speed gradient was able to distinguish changes in intrinsic stiffness from those induced by differing hemodynamic load (a speed of  $\pm 3.2$  m/s in parasternal short-axis (PSAX) view was associated with a wave speed gradient of  $-0.17 \pm 0.15$  m/s/mm when pressure was elevated compared to  $0.04 \pm 0.05$  m/s/mm when stiffness was elevated). The gradient however decreased when stiffness increased (decrease with a factor 3 in PSAX when stiffness doubled at 20 mmHg). The human data analysis confirmed the presence of a wave speed gradient in a patient with elevated ventricular pressure. *Conclusion:* Cardiac SWE modeling is a useful tool to gain additional insights into the complex wave physics and to guide post-processing. The transmural differences in wave speed may help to distinguish loading-induced stiffening from intrinsic stiffness changes. *Significance:* The transmural wave speed gradient has potential as a new diagnostic parameter for future clinical studies.

**Index Terms—**cardiac shear wave elastography, finite element model, hemodynamic loading, intrinsic stiffness, operational stiffness

This work was supported by the Research Foundation Flanders (FWO) under grant 1211620N to Annette Caenen. The computational resources (Stevin Supercomputer Infrastructure) and services used in this work were provided by the VSC (Flemish Supercomputer Center), funded by Ghent University, FWO and the Flemish Government – department EWI.

\*Annette Caenen is with the Institute for Biomedical Engineering and Technology, Ghent University, Ghent, Belgium and the Department of Cardiovascular Sciences, KU Leuven, Leuven, Belgium (correspondence e-mail: annette.caenen@ugent.be). Stéphanie Bézy, Aniela Petrescu, Annegret E. Werner, Jens-Uwe Voigt and Jan D'hooge are with the Department of Cardiovascular Sciences, KU Leuven, Leuven, Belgium. Patrick Segers is with the Institute for Biomedical Engineering and Technology, Ghent University, Ghent, Belgium. <sup>#</sup>J. D'hooge and P. Segers are joint last author.

## I. INTRODUCTION

**R**obust, non-invasive methods to assess myocardial stiffness in clinical practice can improve our insights in the pathophysiology of various cardiac diseases; may facilitate diagnostics and can guide treatment and patient follow-up. An ultrasound-based technique with large potential to non-invasively evaluate the mechanical properties of the myocardium is shear wave elastography (SWE). In SWE, one determines the propagation characteristics of shear waves in the tissue of interest, which are directly linked to the tissue's shear modulus under the assumptions of homogeneity, isotropy and linear elasticity. Shear waves in the heart can be naturally present after impulse events such as valve closure [2, 3] or can be externally induced by using an acoustic radiation force (ARF) impulse [4, 5].

Even though recent clinical studies demonstrated the distinguishing power of cardiac SWE for amyloidosis [6], diffuse myocardial injury [7] and hypertrophic cardiomyopathy [8-10], the proper interpretation of cardiac SWE measurements remains complex. This complexity arises from multiple factors affecting SWE, ranging from the selected technical settings (the ultrasound scanner [11], experimental protocol or propagation speed estimation method [12]) to the anatomical and mechanical characteristics of the heart. Cardiac tissue is in essence a thin-walled, non-linear, anisotropic, viscoelastic, actively contracting material, suggesting that shear wave propagation speed might also be geometry-, loading-, frequency-, direction- and contractility-dependent [8, 13-17]. Therefore, an observed increased wave propagation speed might be attributed to an increased myocardial stiffness, but may be equally well explained by an increased strain/stress level, an increased strain rate, an altered fiber orientation or even a shorter push duration in case of ARF-based SWE. Additional complexity arises as cardiac disease is typically associated with cardiac remodeling, where multiple mechanical factors might change simultaneously.

It was previously shown in a pre-clinical *in vivo* study in pigs that an increased preload can affect shear wave propagation speed, especially in an infarcted heart [14]. Cvijic et al. [10] therefore suggested to normalize myocardial

stiffness assessed with SWE to wall stress in order to account for load-dependency. However, as it is difficult to accurately assess wall stress non-invasively and human/animal experiments encompass all confounding factors that complicate SWE simultaneously, we developed a computational model of cardiac SWE in the pressurized LV based on the finite element method (FEM). We performed FEM simulations for an isotropic and an anisotropic material model of an idealized LV model to study the interplay between pressure and myocardial stiffness. The model provided unique access to the instantaneous stiffness changes, which are related to the wave propagation patterns in this study. The simulation outcomes inspired and triggered additional SWE processing on human data to verify our numerical findings.

## II. MATERIALS AND METHODS

### A. Geometry and material model

The left ventricle was modeled as a prolate spheroid [18], with an inner major ellipse axis of 40.9 mm, an inner minor ellipse axis of 19.7 mm and a uniform thickness of 12.0 mm, truncated at 19.0 mm distance from the center of the ellipsoid (Fig. 1). These unloaded dimensions were chosen such that the loaded global model in end-diastolic state corresponded to the reported echocardiographic range of healthy adults in end-diastole (diameter of  $50.2 \pm 4.1$  mm, volume of  $106 \pm 22$  ml and wall thickness of  $0.8 \pm 0.2$  mm) [19, 20]. As transthoracic SWE *in vivo* is typically performed in the interventricular septum (IVS), we considered a segment of the truncated prolate spheroid model (one third of the circumference of the circular

cross-section), representing the IVS, with symmetry boundary conditions in the angular direction at the edges of the segment. The basal surface was only free to move in the radial direction.

As the left ventricular wall is a composite of sheets of parallel myocytes, we adopt the classical Holzapfel-Ogden model [21] for the passive material response with strain energy function  $\psi$ :

$$\psi = \frac{1}{D} \left( \frac{J^2 - 1}{2} - \ln(J) \right) + \frac{a}{2b} \exp[b(I_1 - 3)] + \sum_{i=f,s} \frac{a_i}{2b_i} \{ \exp[b_i(I_{4i} - 1)^2] - 1 \} + \frac{a_{fs}}{2b_{fs}} [ \exp(b_{fs} I_{8fs}^2) - 1 ] \quad (1)$$

where  $J$  is the elastic volume ratio;  $I_1$ ,  $I_{4f}$ ,  $I_{4s}$  and  $I_{8fs}$  are the deviatoric invariants of the left and right Cauchy-Green deformation tensors with subscript  $f$ ,  $s$  and  $fs$  denoting the fiber contribution, sheet contribution and the coupled fiber sheet contribution; and  $a$ ,  $b$ ,  $a_f$ ,  $b_f$ ,  $a_s$ ,  $b_s$ ,  $a_{fs}$ ,  $b_{fs}$  and  $D$  are the nine material unknowns. We considered an isotropic and anisotropic Holzapfel-Ogden model, with its parameters based on values reported in literature [1] and given in Table 1. The fiber orientation in the anisotropic material model varied from  $+70^\circ$  at the LV side to  $-50^\circ$  at the RV side [22], as illustrated in Fig. 2. This figure shows the meaning of local fiber axis  $f$ , sheet axis  $s$  and sheet-normal axis  $n$  for a sheet at mid-wall thickness.

The mechanical response of these material models were compared in terms of (i) the stress-stretch response, by simulating a biaxial test on a beam-shaped sample (10x10x12 mm in longitudinal-circumferential-radial direction) while

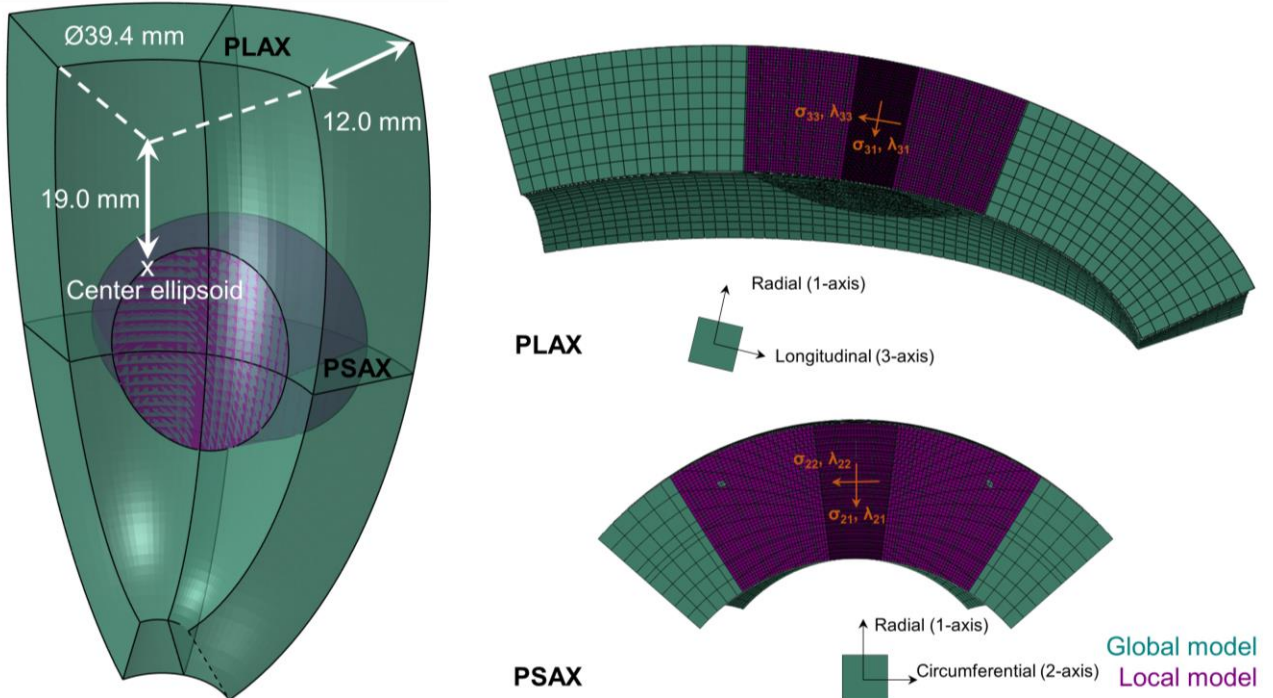


Fig. 1. Mesh geometry of global and local model in 3D, parasternal long axis (PLAX) and parasternal short axis (PSAX) view. Stresses and strains are calculated in a local Cartesian coordinate system, as indicated for a center element of the local model in PLAX and PSAX.

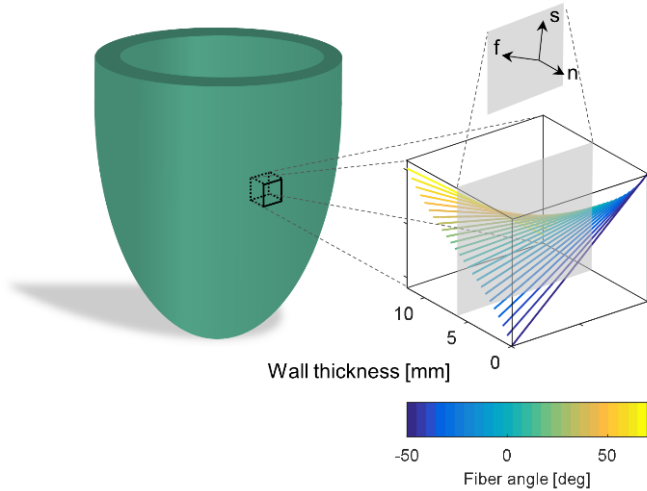


Fig. 2. Fiber orientation of the anisotropic material model: fibers varied from  $-70^\circ$  at the LV side to  $50^\circ$  at the RV side. The local coordinate system  $(f, s, n)$  denotes fiber axis  $f$ , sheet axis  $s$  and sheet-normal axis  $n$ .

increasing stretch from 1.0 to 1.2 in a 1:1 ratio, and (ii) the pressure-volume response, by pressurizing the LV segment with a pressure of 30 mmHg in the LV and 4 mmHg in the RV (total volume was obtained by multiplying the cavity volume of Fig. 1 with a factor 3). For the virtual biaxial test, the Cauchy stress-stretch response for the central element of the beam-shaped sample is analyzed.

### B. SWE simulations in a pressurized ventricle

The SWE simulations mimicked ARF-based SWE as simulating a valve closure event requires to consider the fluid dynamics and the papillary muscle structures, which is beyond the scope of this paper. The simulations were performed in the finite element method (FEM) software Abaqus (Abaqus Inc, Providence, RI, USA) using the explicit solution technique. To solve the two problems of different mechanical (dynamic wave propagation in a few ms vs. ‘static’ ventricle under pressure with pressure build up in a few hundreds of ms) in a computationally efficient way, we considered three different simulation steps. First, quasi-static simulations of the IVS global model in end-diastolic state were performed by applying a LV pressure of 8 mmHg on the inner curved surface of the global model and a RV pressure of 4 mmHg on the outer curved wall of the model. The quasi-static requirement was guaranteed by making sure that the kinetic energy of the simulation did not exceed 5% of the internal energy. The optimized mesh consisted of 11 872 hexahedral solid elements. Second, the node-based submodeling technique of Abaqus was applied to transfer the end-diastolic results of step 1 to that of the local model in Fig. 1, which had (i) a refined mesh to accommodate SWE modeling (10-15 elements per wavelength [23]) and to capture the spatially varying profile of the ARF [24] and (ii) smaller dimensions (about 30 mm in longitudinal and circumferential direction, corresponding to a representative anatomical line length typically used in actual SWE data) to reduce computational time. The local model consisted of 480 000 hexahedral solid elements. Third, wave propagation is simulated after ARF

application. As wave propagation is strongly influenced by its boundaries, we also modeled the surrounding blood as an acoustic medium, of which the acoustic pressure is coupled to the mechanical displacement of the local model. The blood was modeled as finite acoustic layers on both sides of the local model with a thickness of 10 mm, and infinite boundaries were modeled at the infinite edges. A density of  $1050 \text{ kg/m}^3$  and a bulk modulus of 200 MPa were assumed in order to decrease computational time. Infinite structural elements were also modeled at the edges of the local model to absorb all wave energy reaching the outer boundaries of the local model. The ARF was mimicked as a 3D Gaussian body force applied for  $250 \mu\text{s}$  in the axial direction, described according to [25]:

$$ARF(x, y, z) = A \cdot \exp\left(-\left(\frac{(x-x_0)^2}{\sigma_x^2} + \frac{(y-y_0)^2}{\sigma_y^2} + \frac{(z-z_0)^2}{\sigma_z^2}\right)\right) \quad (2)$$

where  $A$  is the maximum magnitude;  $x_0, y_0$  and  $z_0$  are the coordinates of the focal point and  $\sigma_x, \sigma_y$  and  $\sigma_z$  are the Gaussian width in longitudinal, circumferential and longitudinal direction. The focal point was set to the center of the local model (cardiac mid-wall) and the Gaussian widths were  $\sigma_x = \sigma_y = 0.4 \text{ mm}$  and  $\sigma_z = 20 \text{ mm}$ . The maximal magnitude of the ARF force was determined such that a resulting peak displacement of tens of  $\mu\text{m}$  was observed – a typical response for a realistic ARF excitation [26]. Wave propagation was simulated for a period of 4 ms. Simulations were run on high performance clusters (Stevin Supercomputer Infrastructure) using 20 CPUs for approximately 10 mins for step 1 and using 72 CPUs typically taking approximately 23 hours for step 2 and 1 hour for step 3.

The following configurations were considered:

(i) Effect of LV pressure (LVP): for both the isotropic and anisotropic model (see section II.1), LVP was increased from 8 to 20 mmHg, while RV pressure remained 4 mmHg.

(ii) Effect of stiffness: in the anisotropic model, fiber and sheet stiffness (parameters  $a_f$  and  $a_s$ ) are increased by a factor 5, as observed from the collagen thickening in myocardial fibrosis of a spontaneously hypertensive rat model [27]. Similarly, for the isotropic model, the isotropic contribution in the strain energy potential (parameter  $a$ ) was increased with a factor 5. These simulations with elevated stiffness represented myocardial fibrosis. The pressures remained 8 mmHg in the LV and 4 mmHg in the RV.

TABLE I  
SUMMARY OF THE PARAMETERS USED FOR THE ISOTROPIC AND ANISOTROPIC  
HOLZAPFEL-OGDEN MATERIAL MODEL [1]

Parameter	Isotropic	Anisotropic
$a$	1.9812 kPa	0.13034 kPa
$b$	2.5658	3.243
$a_f$	0 kPa	3.2205 kPa
$b_f$	0	3.5845
$a_s$	0 kPa	0.7418 kPa
$b_s$	0	1.5470
$a_{fs}$	0 kPa	0.1799 kPa
$b_{fs}$	0	3.39
$D$	$0.01 \text{ MPa}^{-1}$	$0.01 \text{ MPa}^{-1}$

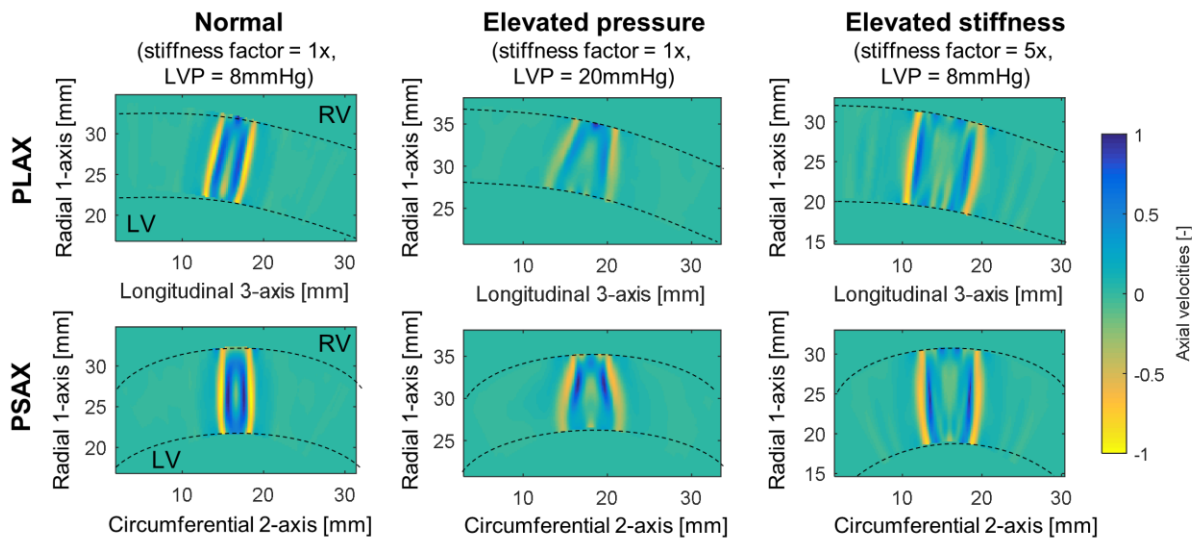


Fig. 3. Normalized axial tissue velocity patterns for the isotropic model in PSAX (bottom) and PLAX (top) at time point 1.5 ms depicting shear wave propagation for a normal heart (left), a heart with elevated pressure (middle) and a heart with elevated stiffness (right). Movies are provided as online supplementary material.

### C. Transmural SWE and stress-stretch analysis

Shear wave propagation was analyzed in tissue velocity data, which was extracted from Abaqus at a sampling rate of 25 kHz and subsequently linearly interpolated to an equidistant polar grid ( $\Delta r = \Delta z = 0.02$  mm and  $\Delta \theta = 5^\circ$ ). As no actual SWE experiments with the selected ARF settings were performed, we refrained from reporting absolute tissue velocities and normalized velocity data with respect to the maximal absolute tissue velocity. We focused on two typically used echocardiographic views for SWE, i.e. the parasternal long-axis (PLAX) and parasternal short-axis (PSAX) view. Wave propagation speed was then determined for 10 equally spread splines across the cardiac wall thickness (with the same distance from the epi- and endocardial border as in between the splines) using the Radon transform [28], yielding the most likely linear trajectory along which the wave travels. Transmural wave speed gradients were calculated as the average of the instantaneous speed change across the cardiac

wall divided by the wall thickness.

Next to the wave speed assessment, we studied how the operational stiffness varied (i.e. the local slope of the stress-stretch relation). Therefore, we analyzed the slope of the tangent to the Cauchy shear stress-stretch relation in the quasi-static procedure of pressurizing the ventricle in the global model (higher temporal resolution than the local model). As the local model is limited in size, we performed this procedure for multiple locations throughout the cardiac wall in the ARF focal zone and assumed that this analysis was representative for the local stiffness of the complete local model. More specifically, we studied the transmural changes in Cauchy shear stress and stretch in the direction of the tissue motion ( $\lambda_{21}, \sigma_{21}$ ) in PSAX and ( $\lambda_{31}, \sigma_{31}$ ) in PLAX according to a local Cartesian coordinate system in each element, as demonstrated in Fig. 1. Transmural shear stiffness gradients were calculated as the average of the instantaneous stiffness change across the cardiac wall divided by the wall thickness.

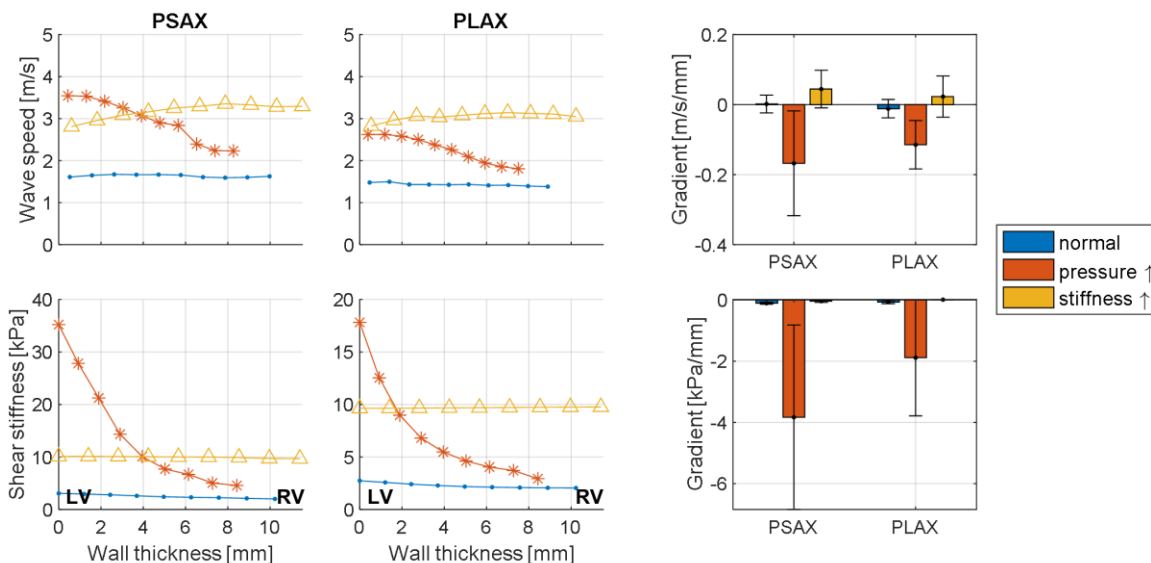


Fig. 4. Transmural changes in wave speed (derived from SWE analysis) and shear stiffness (derived from stress-stretch analysis) in parasternal short axis (PSAX) and parasternal long axis (PLAX) view for the isotropic simulations.

#### D. Validating numerical findings in human subjects

To validate our numerical findings, we investigated the transmural changes in cardiac wave propagation speed in human subjects. As ARF-based SWE is not yet routinely applied in the clinics because of low success rates and the requirement of an ultrasound scanner with sufficient power supply, we analyzed the mechanical waves occurring in the IVS after mitral valve closure (MVC). To analyze these waves, we are restricted to the PLAX view as this view detects tissue motion along the ultrasound beam and transverse to the cardiac wall (hence a ‘shear’ wave) while including the source of wave excitation. We considered three human subjects from completed and ongoing studies at the KULeuven with clinical parameters tabulated in table II: one healthy volunteer (representative case for normal pressure and myocardial stiffness), one heart failure patient with LV end-diastolic pressure of 24 mmHg due to a previous myocardial infarct – while contraction pattern and wall thickness remained normal (representative case for elevated pressure) and one heart transplant patient with confirmed diffuse myocardial fibrosis on MRI (native T1 relaxation time of 1064 ms was measured, which is larger than the cut-off of 1040 ms for fibrosis [7]) and a normal pulmonary capillary wedge pressure of 12 mmHg (representative case for elevated stiffness). All subjects were scanned by an experienced clinician using an experimental ultrasound scanner HD-PULSE [29] following a protocol approved by the ethical committee of the University Hospital of Leuven. SWE data were acquired using a commercial cardiac 3.5 MHz phased array (P2-5AC, Samsung

TABLE II  
CLINICAL PARAMETERS (HV = HEALTHY VOLUNTEER; HF = HEART FAILURE;  
HTX = HEART TRANSPLANT)

Patient	Age [yrs]	Gender	LV ejection fraction [%]	Septal wall thickness [cm]
HV	27	M	60	1.0
HF	86	F	43	1.2
HTX	37	M	59	1.3

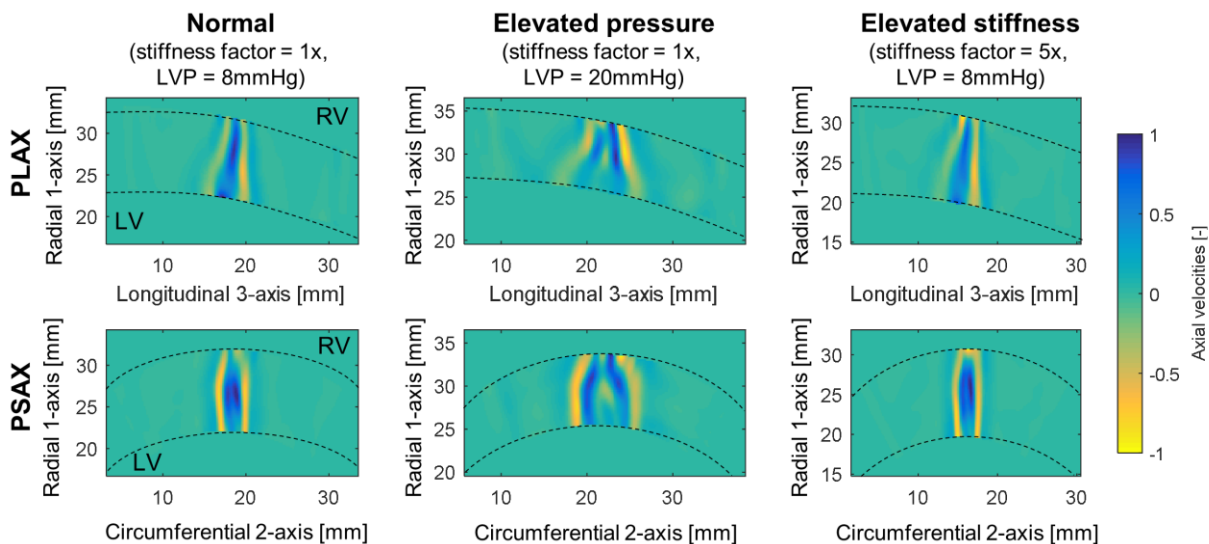


Fig. 6. Normalized axial tissue velocity patterns for the anisotropic model in PSAX (bottom) and PLAX (top) at time point 1.5 ms depicting shear wave propagation for a normal heart (left), a heart with elevated pressure (middle) and a heart with elevated stiffness (right). Movies are provided as online supplementary material.

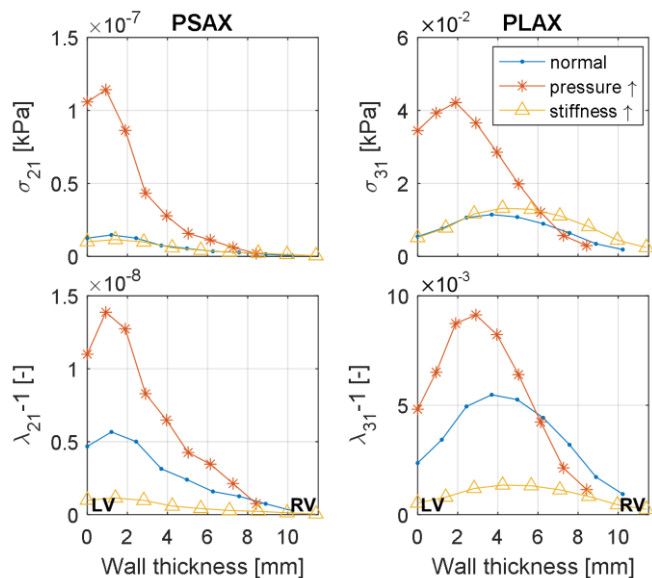


Fig. 5. Transmural changes in shear stresses and stretches, extracted from the isotropic simulation results, in PSAX and PLAX. The orientation of the stresses and stretches are indicated in Fig. 1.

Medison, Seoul, South Korea) at a frame rate of 941 Hz through the compounding of 6 diverging waves [30]. SWE data was analyzed by a clinical researcher experienced in this type of measurements using the custom-made software tool SPEQLE (version 4.6.8, KU Leuven), where wave speeds are determined using a cross-correlation algorithm [6] (we refer to [30] for more information on the post-processing settings).

This study used retrospective data of a clinical study that was approved by the local ethics committee of KULeuven (EC-number s60439), for which all subjects gave written informed consent.

#### E. Sensitivity analysis

The sensitivity of our transmural SWE and strain-stress analysis was further explored by performing additional simulations in which stiffness and pressure were further altered. We considered 3 stiffness factors (1x, 2x and 5x) and

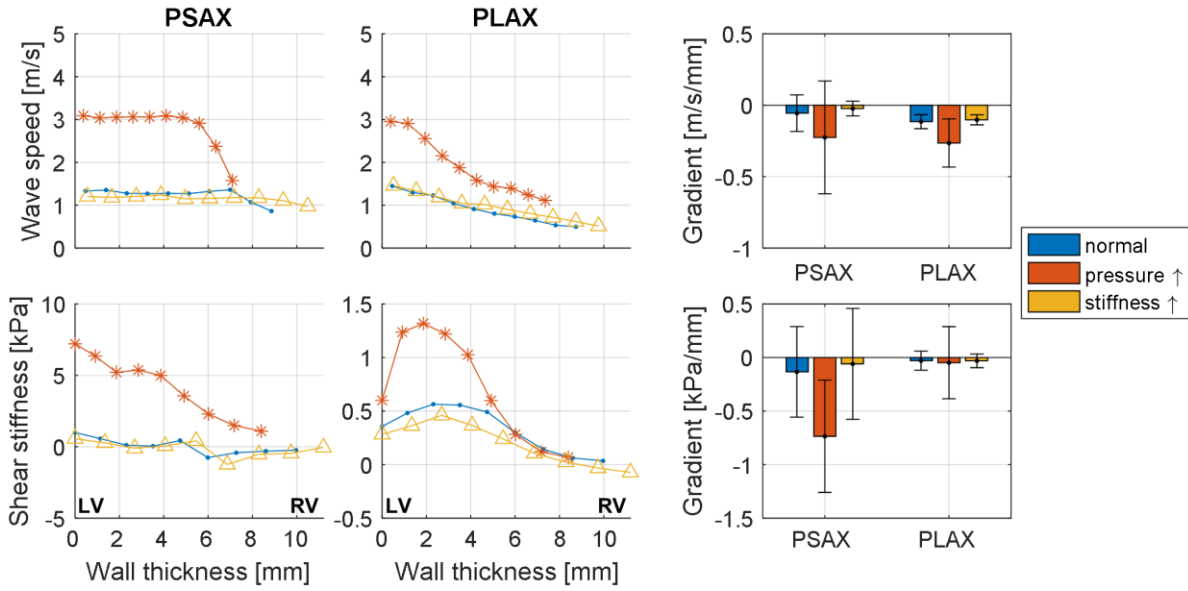


Fig. 7. Transmural changes in wave speed (derived from SWE analysis) and shear stiffness (derived from stress-stretch analysis) in PSAX and PLAX for the anisotropic simulations.

3 LVPs (8, 20, and 30 mmHg), resulting in a total of 9 simulations. Correlation between shear wave speed and shear stiffness was determined by computing Pearson's linear correlation coefficient.

### III. RESULTS

#### A. SWE in the isotropic LV model

The resulting wave propagation patterns in the normal model are shown in Fig. 3 for two common echocardiographic views, PLAX and PSAX, alongside those observed at an elevated pressure and elevated myocardial stiffness. The shear waves are clearly propagating faster when pressure or stiffness is elevated, but we also notice a more curved wave front for the elevated pressure case: the wave propagates faster along the LV side than along the RV side.

This observation is confirmed when analyzing the transmural wave speed variations, as can be seen in the upper panels of Fig. 4. The wave speed at mid-wall is 1.67 and 1.43 m/s for the normal heart, 3.07 and 2.38 m/s for the heart with elevated pressure and 3.25 and 3.08 m/s for the heart with elevated myocardial stiffness for PSAX and PLAX respectively. Taking into account the thickness of each model (see Table III), the transmural wave speed gradient is calculated. The average transmural wave speed gradient for the elevated pressure simulation ( $-0.17 \pm 0.15$  m/s/mm in PSAX and  $-0.11 \pm 0.07$  m/s/mm in PLAX) is larger in absolute value than that for the normal simulation ( $0.002 \pm 0.025$  m/s/mm in

PSAX and  $-0.012 \pm 0.026$  m/s/mm in PLAX) and elevated stiffness simulation ( $0.04 \pm 0.05$  m/s/mm in PSAX and  $0.02 \pm 0.06$  m/s/mm in PLAX). These patterns are also reflected in the transmural instantaneous stiffness changes, which are depicted in the lower panels of Fig. 4. The transmural shear stiffness patterns show a clear gradient for the heart with elevated pressure (average of  $-3.8 \pm 3.0$  kPa/mm in PSAX and  $-1.9 \pm 1.9$  kPa/mm in PLAX), whereas the normal heart and the heart with elevated stiffness show minimal transmural instantaneous stiffness changes for both echocardiographic views ( $< 0.11$  kPa/mm in absolute value).

The increased transmural gradient in operational shear stiffness for the elevated pressure case reflects the transmural shear Cauchy stress changes across the cardiac wall in the upper panels of Fig. 5. The shear Cauchy stress  $\sigma_{21}$  is minimal (order of  $10^{-7}$  kPa), but for  $\sigma_{31}$ , a transmural change of 0.04

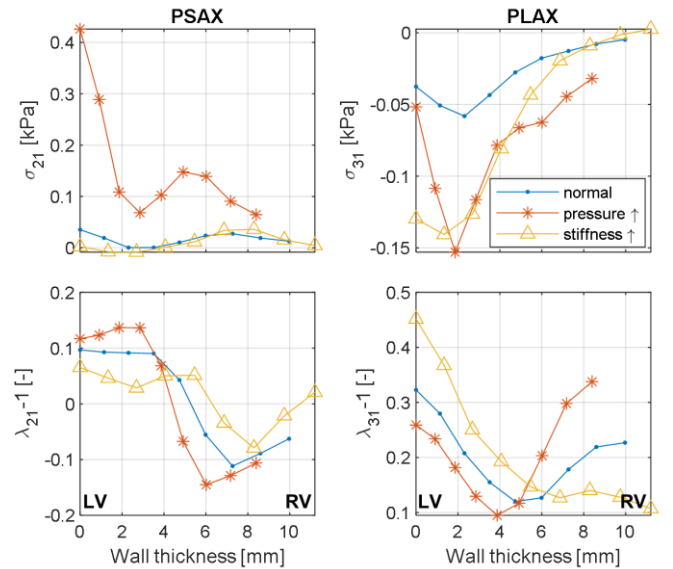


Fig. 8. Transmural changes in shear stresses and stretches, extracted from the anisotropic simulation results, in PSAX and PLAX. The orientation of the stresses and stretches are indicated in Fig. 1.

TABLE III

THICKNESS AND RADIUS OF CURVATURE OF ISOTROPIC AND ANISOTROPIC MODELS

	Isotropic		Anisotropic		
	Thick-ness [mm]	Radius of curvature [mm]	Thick-ness [mm]	Radius of curvature [mm]	
	PSAX	PLAX	PSAX	PLAX	
Normal	10.0	22.0	10.0	22.1	45.3
Pressure ↑	8.2	26.8	8.4	25.7	50.8
Stiffness ↑	11.5	19.3	11.2	19.7	45.3

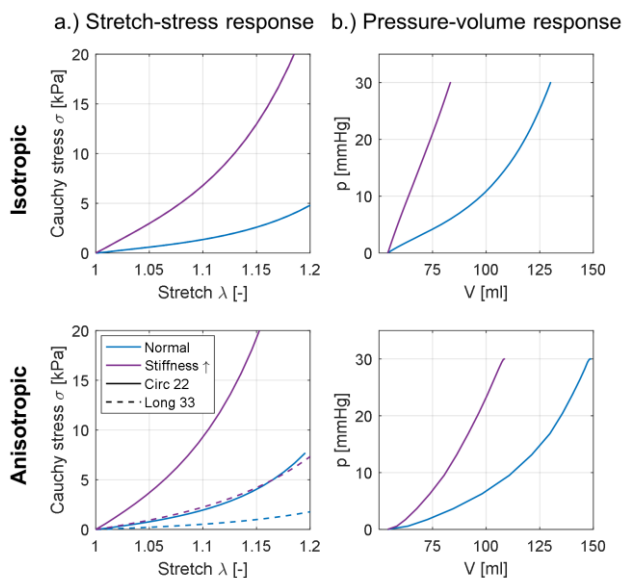


Fig. 9. Mechanical response of the normal and fibrotic material models in case of isotropy and anisotropy: (a) Cauchy stress-stretch curves for the central element in circumferential and longitudinal direction during virtual biaxial testing (applying a stretch of 1.2 in the circumferential and longitudinal direction simultaneously). (b) Pressure-volume response while applying a pressure of 30 mmHg in the LV and 4 mmHg in the RV.

kPa in Cauchy stress was observed when pressure increased, compared to 0.01 kPa for the normal simulated heart. The shear stretch also varied, as shown in the lower panels of Fig. 5, but the transmural trend remained similar as for the normal simulation. For the simulated heart with elevated stiffness, the transmural stresses remained the same as for the normal simulated heart whereas the cardiac wall became less stretched (stretch  $\lambda$  close to 1).

### B. SWE in the anisotropic LV model

The wave propagation patterns for the anisotropic model are illustrated in Fig. 6 for the three considered cases. As for the isotropic material model, we notice that the shear waves propagate faster closer to the LV side than the RV side when the pressure is elevated. However, the fibrotic wave propagation pattern does not depict any perceptible differences compared to that of the normal heart.

The wave speed measured at mid-wall is 1.27 and 0.91 m/s for the normal heart, 3.06 and 1.87 m/s for the heart with elevated pressure and 1.15 and 1.01 m/s for the heart with elevated myocardial stiffness for PSAX and PLAX

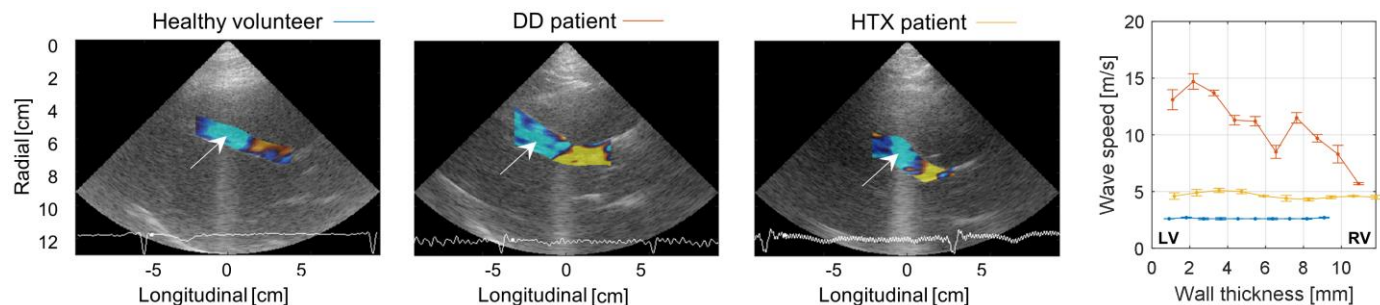


Fig. 10. Transmural changes in wave front (1 time instance) and speed for human subjects in the parasternal long axis view (PLAX): healthy volunteer, diastolic dysfunction (DD) patient with elevated pressure and heart transplant (HTX) patient with confirmed fibrosis. The arrow indicates the tracked wave front.

respectively (see Fig. 7). When analyzing the wave speed gradients across cardiac wall thickness (see Table III), the largest gradient is observed for the simulated heart with elevated pressure ( $-0.23 \pm 0.40$  m/s/mm in PSAX and  $-0.26 \pm 0.17$  m/s/mm in PLAX) compared to the normal heart ( $-0.06 \pm 0.13$  m/s/mm in PSAX and  $-0.11 \pm 0.05$  m/s/mm in PLAX) and the fibrotic heart ( $-0.02 \pm 0.05$  m/s/mm in PSAX and  $-0.10 \pm 0.04$  m/s/mm in PLAX). The shear stiffness gradient is also largest in magnitude when LV pressure is elevated ( $-0.74 \pm 0.52$  kPa/mm in PSAX and  $-0.05 \pm 0.34$  kPa/mm in PLAX), for other cases the absolute gradient is less than 0.13 kPa/mm in PSAX and 0.03 kPa/mm in PLAX.

The transmural gradient in shear Cauchy stress  $\sigma_{21}$  is largest for the elevated pressure case in PSAX (transmural stress change of 0.37 kPa compared to 0.04 kPa for the normal and fibrotic heart), whereas the transmural change in shear Cauchy stress  $\sigma_{31}$  in PLAX is 0.12 kPa for the simulations with elevated pressure and stiffness compared to 0.06 kPa for the normal simulated heart (see Fig. 8). The shear stretches are illustrated in the lower panels of Fig. 8. In PSAX, the ventricle is more stretched when LV pressure increases ( $\lambda \gg 1$  or  $\lambda \ll 1$ ) and less stretched when myocardial stiffness increases ( $\lambda$  closer to 1). In PLAX, the stretches are on average the same for all three considered cases.

### C. Mechanical response of isotropic and anisotropic material model

The material response of the anisotropic model is compared to that of the isotropic model in Fig. 9a for the normal and fibrotic material model during virtual biaxial testing. The anisotropic simulations clearly show a stiffer mechanical behavior for the circumferential direction than the longitudinal direction due to the fiber orientation. The fibrotic response is stiffer than the normal response in all directions and for both isotropic and anisotropic simulations. The pressure-volume curves of the four material laws in a LV model confirm the observations of the virtual biaxial test (see Fig. 9b). We should however note that the stretch-stress response for the isotropic model is less stiff than for the anisotropic model, whereas the pressure-volume response is reversed.

### D. SWE in human subjects

The wave propagation is shown in the 3 left panels of Fig. 10 at 1 time points for all 3 subjects. The transmural wave speed results in human subjects are depicted in the right panel

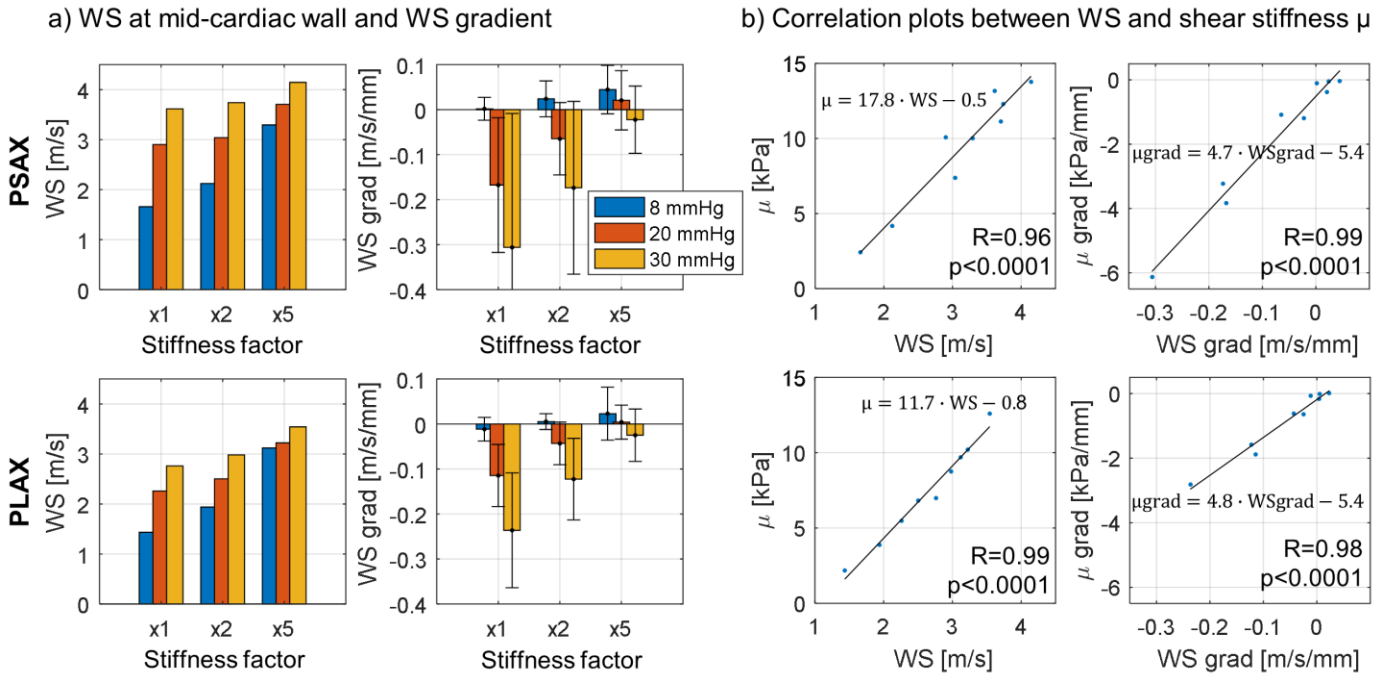


Fig. 11. Sensitivity analysis for the isotropic model depicting changes in wave speed (WS) at mid cardiac wall and WS gradient in panel a and showing correlation plots between shear stiffness vs. WS and shear stiffness gradient vs. WS gradient in panel b.

of Fig. 10. The wave speeds at mid-wall are  $2.6 \pm 0.1$  m/s for the healthy volunteer,  $8.5 \pm 0.6$  m/s for the patient with elevated pressure (24 mmHg) and  $4.4 \pm 0.1$  m/s for the patient with myocardial fibrosis in PLAX. The patient with elevated LV pressure had the largest wave speed gradient ( $0.75 \pm 1.82$  m/s/mm), compared to the healthy volunteer ( $0.01 \pm 0.07$  m/s/mm) and the patient with myocardial fibrosis ( $0.01 \pm 0.19$  m/s/mm).

#### E. Sensitivity analysis

As the considered anisotropic simulations did not show an increase in wave speed when stiffness increased, the sensitivity analysis considering three different LVPs and stiffness factors was only performed for the isotropic material model. Fig. 11a shows the combined effect of elevated stiffness and pressure on wave speed and wave speed gradient. Wave speed at mid-wall increases further when pressure was elevated for every considered material stiffness (e.g. 1.66, 2.90 and 3.62 m/s for stiffness factor 1 vs. 3.29, 3.70 and 4.15 m/s for stiffness factor 5 in PLAX at EDP levels of 8, 20 and 30 mmHg, respectively). For the wave speed gradient, we observed that the gradient is minimal when the largest LV EDP is applied for the considered material stiffness. However, the absolute speed gradient decreases when stiffness increases (e.g.  $-0.31 \pm 0.30$ ,  $-0.17 \pm 0.19$  and  $-0.02 \pm 0.07$  m/s/mm at LV EDP of 30 mmHg in PLAX for stiffness factor 1, 2 and 5 respectively). Fig. 11b illustrates a very strong and significant correlation between shear stiffness and wave speed ( $R=0.96$  in PSAX and  $R=0.99$  in PLAX;  $p<0.0001$ ) and between shear stiffness gradient and wave speed gradient ( $R=0.98$  in PSAX and  $R=0.98$  in PLAX;  $p<0.0001$ ). Even though stiffness and pressure both influence wave speed and wave speed gradient, the strong correlations demonstrate the direct mechanical meaning.

## IV. DISCUSSION

### A. SWE simulations in a pressurized left ventricle

This work studied the simulated wave propagation patterns that arise in the IVS when pressure or myocardial stiffness is elevated, in comparison to normal pressure and stiffness. Analysis of multiple wave propagation paths across the cardiac wall allowed to assess the transmural gradient in wave speed, next to the conventionally assessed parameter in cardiac SWE, i.e. wave speed at mid-wall. Wave speed increased when pressure or myocardial stiffness was elevated (e.g. +66.6% when pressure increased 12 mmHg vs. 115.9% when stiffness increased with a factor 5 in the isotropic simulations; +105.6% when pressure increased 12 mmHg in the anisotropic simulations in PLAX); but the absolute wave speed gradient across the wall was the largest when LV pressure rose (+89.9% for the isotropic simulations and +130.4% for the anisotropic simulations compared to the normal model in PLAX). Here, we should note that the anisotropic material model of myocardial fibrosis from literature [27] was not able to generate an upturn in wave speed and shear stiffness as expected; which is further discussed in section IV.B. The sensitivity analysis of the transmural wave speed gradient parameter in the isotropic simulations (Fig. 11) revealed that the discriminating power of the transmural wave speed gradient for elevated pressure decreased when the intrinsic stiffness increased: the wave speed gradient decreased with 48.1% in PLAX and 43.2% in PSAX when stiffness increased with a factor 2 for a pressure difference of 22 mmHg.

In general, the transmural wave speed changes followed a similar pattern as the operational stiffness gradient derived from the internal shear stresses and stretches (see Fig. 4 and

Fig. 7). There are however some discrepancies between the two transmural trends, which might be explained by (i) the effect of the geometry on wave propagation (see supplementary material on phase speed analysis), (ii) the complex loading condition, as other stress/stretch components – especially in the direction of wave propagation – might also affect wave propagation [31], and (iii) potential wave mode coupling. Despite these potential influences on the link between SWE and instantaneous shear stiffness, the sensitivity analysis in the isotropic simulations showed an excellent correlation (min.  $R$  of 0.96 in Fig. 11) between wave speed and shear stiffness on the one hand, and wave speed gradient and shear stiffness gradient on the other hand – demonstrating their direct mechanical meaning.

We used the findings from the simulations to guide processing of SWE data in human subjects; and consequently, analyzed the transmural wave speed gradient in a healthy volunteer, a patient with elevated pressure (24 mmHg) and a patient with confirmed fibrosis on MRI. This analysis confirmed the observations in the simulations (see Fig. 10) and demonstrated the potential of using transmural speed gradient as discriminator between elevated pressure and elevated myocardial stiffness.

The reported speeds for the healthy heart model (1.67 and 1.43 m/s for the isotropic model and 1.27 and 0.91 m/s for the anisotropic model for PLAX and PSAX respectively) are within the ranges documented in literature. A wide variety in end-diastolic speed (0.82-2.65 m/s) has been reported for ARF-based SWE in preclinical studies [16, 32-34]. Villemain et al. [8] reported  $1.45 \pm 0.26$  m/s (PLAX) and  $1.96 \pm 0.38$  m/s (PSAX) for adult healthy volunteers ( $n=60$ ), showing higher speeds in PSAX than in PLAX, similar as observed in the models.

The effect of loading on wave propagation speed has been extensively studied in a non-cardiac context, where the difference in wave speed in a nonlinear elastic material at different uniaxial stress levels is used to evaluate tissue nonlinearity (also called the theory of acoustoelasticity in literature [35-39]). These studies all assume a-priori knowledge of material model and loading status in order to eliminate the loading bias from the stiffness estimation, but this is not known in cardiac SWE. Therefore, we previously explored the effect of uniaxial stress on wave propagation patterns in cardiac tissue using FEM models [40] (together with complementary ex vivo experiments [41]); but now we investigated for the first time the effect of a more complex and realistic cardiac loading pattern on simulated shear waves in an idealized LV model. The results of our model are in line with previous ARF-based SWE studies which showed an increase in speed when preload is increased in a healthy animal heart [14, 16], and this speed increase became more pronounced when myocardial fibrosis is present [14]. A magnetic resonance elastography *in vivo* study in pigs even suggested a linear dependence between end-diastolic stiffness

and LV pressure [42]. Even though the reported wave speed values for the elevated pressure simulation are rather high compared to what has been reported before (an increase of 1.0 m/s for the isotropic and anisotropic model at cardiac mid-wall in PLAX compared to  $+0.3$  m/s<sup>1</sup> in [14] and  $+0.5$  kPa<sup>2</sup> in [16] in long-axis views), it should be noted that previous animal studies did not take into account the transmural speed variations, are tracking another cardiac wall [14, 16], are an ex vivo preparation [16] and/or use a different spectral content of the wave [14]. Furthermore, an *in vivo* study of natural SWE in pigs showed an increase of about 2 m/s when LV pressure increased with  $\pm 2$  mmHg [15]. The model has however limitations which are discussed in section IV.D.

#### B. Wave propagation in an isotropic vs. anisotropic material model

As LV geometry, loading conditions and material anisotropy can all affect wave propagation patterns, we increased the complexity of the FEM model gradually in order to better understand the wave physics. In previous work, we have shown that solely LV geometry can affect the transmural wave speed estimations depending on transmural depth, LV zone and echocardiographic view analyzed due to dispersion effects [13]. These dependencies are again observed in Fig. 4, where we looked at the combined effect of LV geometry and loading (in combination with material nonlinearity) on wave propagation. A more detailed phase velocity analysis of the isotropic simulations can be found in the online appendix, where it was shown that the spectral content of the wave and the intrinsic dispersion relations altered when stiffness or pressure changed. Even though the frequency-dependent phase velocity clearly demonstrated the presence of dispersion, the group speed estimated from these phase velocities corresponded well with the speed estimated in the time domain.

Efforts have been made in the past to investigate the influence of myocardial anisotropy on wave propagation in FEM models [24, 43]: mechanical waves propagate faster along the fiber than across, resulting in elliptical shaped shear wave patterns, of which the orientation of its major axis changes across the cardiac wall. It is generally accepted in literature [8, 44] that the wave propagation speed at the cardiac mid-wall in PSAX is higher than the wave propagation speed at cardiac mid-wall in PLAX, due to the fiber architecture. However, our models showed that the wave propagation speed in PSAX was higher than in PLAX – even in the isotropic model (1.67 vs. 1.43 m/s at mid-wall in Fig. 4). This corresponded to the increased shear stiffness observed in PSAX (10.1 kPa) compared to PLAX (5.5 kPa) at mid-wall, probably due to the shape of the LV: the circular shape in PSAX will evoke a stiffer response than the ellipsoidal shape in PLAX. Furthermore, the transmural variations in wave speed are in literature [33, 45] typically attributed to the transmural varying fiber orientation, whereas this work shows that the pressure gradient across the wall can also affect the

<sup>1</sup> Speed  $c$  was obtained by converting shear elasticity values  $\mu$  using  $\mu = \rho c^2$  with tissue density  $\rho$  of 1000 kg/m<sup>3</sup>.

<sup>2</sup> Elasticity could not be converted to speed, as it was derived from fitting a viscoelastic model to phase velocity curves.

transmural wave speed estimations (see elevated pressure simulation in the anisotropic model in Fig. 7). It should be noted that even though a pressure difference of 4 mmHg was present across the cardiac wall in the normal simulation (resulting in a shear stiffness difference of 1.1 kPa in PSAX and 0.7 kPa in PLAX for the isotropic model and 6.1 kPa in PSAX and 1.2 kPa in PLAX for the anisotropic model), SWE was not able to pick up these changes in the isotropic model. The interplay between fiber orientation, pressure and geometry and their effect on the transmural varying wave propagation speed should be further investigated in future work. One important difference between the effect of transmural fiber orientation and pressure should be kept in mind: the fiber orientation is derived from the echocardiographic view giving the maximum wave speed at one specific depth, whereas the pressure gradient is reflected in the transmural wave speed variations in one specific echocardiographic view.

Despite the stiffer stretch-stress and pressure-volume response shown in Fig. 9 for the fibrotic material model, the fibrotic anisotropic model was not capable to model the increase in wave speed, as expected in a disease state such as myocardial fibrosis [8]. This is reflected in the shear stiffness, which was also not altered compared to the healthy heart in Fig. 7. Even though the choices of our material parameters for fibrosis are based on previous experiments studying the collagen thickening of a spontaneously hypertensive heart model (increase of  $a_f$  and  $a_s$  with factor 5) [1, 27], it seems that the material model of myocardial fibrosis is incomplete. It should be noted that we did not include a stiffness increase in the sheet-normal direction with a factor 10 – as described by Wang et al. [27] – as this term is not included in the original Holzapfel-Ogden material law. Also, using another frequently reported definition of the fsn-orientation in the Holzapfel-Ogden law (switching s- and n-axis in Fig. 2 [46]) did not affect our study results and conclusions (results not shown). However, it does highlight that the terms in the s-direction and fs-direction contribute minimal to the total mechanical response for SWE. This material model thus deserves further study in the field of SWE, but this is outside the scope of current study. For the isotropic simulations, increasing the isotropic stiffness of the Holzapfel-Ogden material law with a factor 5 did allow us to realistically model myocardial fibrosis. The interplay between pressure, mechanical properties (anisotropy and stiffness) and geometry, needs to be investigated in future studies.

### C. Clinical perspective

The HTX patient with myocardial fibrosis showed a higher wave speed than normal ( $5.91 \pm 0.05$  m/s vs.  $2.60 \pm 0.09$  m/s) whereas the wave speed gradient did not alter (both  $0.01$  m/s/mm). The HF patient with elevated pressure showed a higher wave speed than normal ( $11.20 \pm 0.41$  m/s vs.  $2.60 \pm 0.09$  m/s) and a higher wave speed gradient ( $0.75 \pm 1.82$  m/s/mm vs.  $0.01 \pm 0.07$  m/s/mm). It should be noted that this last patient was substantially older than the other two subjects (see Table 2), which partly explains the increased wave propagation

speed as shown in [6] (increase of 1.26 m/s from age group 20-39 years to age group 60-80 years has been reported). These preliminary clinical results are in line with the simulations regardless of the differences in SWE after MVC – used in the human subjects – and ARF-based SWE – used in the simulations – such as timing in the cardiac cycle, SWE excitation source and selected post-processing settings (tissue accelerations vs. tissue velocities; cross-correlation vs. Radon transform for wave speed estimation), which may explain the observed differences in wave speed magnitude between simulation and patient data. Despite these differences between both techniques, the observed trends in wave speed are similar for both techniques, suggesting that a transmural wave speed gradient is related to a transmural pressure gradient. One should keep in mind that multiple mechanical factors typically change together in patients and cannot be separated as is done in the simulations. The simulations however provided the ideal platform to investigate separately the effect of each mechanical factor on the wave physics.

Current clinical practice in cardiac SWE typically uses one M-mode line along the center of the cardiac wall to estimate the wave propagation speed [6, 8, 10]. Even though previous work suggested a preload-independence of diastolic wave speed [16], this work suggests that diastolic wave speed rather relates to the instantaneous stiffness instead of the intrinsic myocardial stiffness properties. Preliminary results of in-vivo pig experiments confirm these findings for natural SWE [15] and ARF-based SWE [47], but its feasibility needs to be further investigated for realistic pressure changes in cardiac disease.

This work recommends to repeat the wave speed estimation procedure for multiple locations throughout the cardiac wall to estimate the wave speed gradient. Based on the simulation results, it is difficult to put a preferred echocardiographic view forward as both PSAX and PLAX view showed a similar sensitivity for the wave speed gradient to the shear stiffness gradient (similar slope of linear regression fits in Fig. 11b), but it should be kept in mind that the PLAX view is less sensitive to the transmural varying fiber orientation (see Fig. 3 in [40]). Even though the preliminary clinical results in this study are promising, data analysis was limited as only one SWE acquisition with a clear wave propagation over the complete cardiac wall thickness was available per patient. Additionally, the sensitivity analysis showed that a combination of increased stiffness and pressure diminished the predicting power of the wave speed gradient parameter for elevated pressure. This might mean that wave speed in combination with wave speed gradient might be particularly useful to evaluate patients with early diastolic dysfunction, in which there is no excessive cardiac remodeling. Therefore, SWE might be useful as screening tool for diastolic dysfunction. Dedicated studies should be set up to confirm the findings reported here, but also to elaborately investigate *in vivo* feasibility and potentially formulate general recommendations for a robust and consistent estimation of the wave speed gradient parameter. In a next phase, large-scale patient studies are needed to determine a wave speed gradient

threshold for different patient groups.

#### D. Limitations and outlook

Although the current simulation framework yielded realistic wave propagation results, it has a few limitations. First, the implemented Holzapfel-Ogden material law represented the passive material behavior in end-diastole but did not take into account the heart's viscoelastic behavior. As viscosity is known to play a role in SWE – it acts as a low pass filter for wave propagation [48] - future work should assess this effect by implementing a viscoelastic orthotropic material law for the heart [49]. It should also be noted that the out-of-plane fiber orientation [22] was not considered in this work. Furthermore, the current framework should be extended in the future to incorporate the actual LV morphology, tissue surrounding and active contraction to model SWE in an *in silico* beating heart. Second, a real validation of the simulation framework is lacking, but previous simulations using the same numerical framework were validated in plates [50], (unpressurized) LV-models [13] and an (unpressurized) myocardial slab [24]. Furthermore, detecting the same observations in human subjects as in the simulations supports the realism of the simulations.

With the current available 2D SWE technology, clinical studies have mainly focused on the IVS which is located not too deep neither too shallow for generating and tracking waves [6-10]. Therefore, this study focused on the IVS, but we expect that the general findings of this study can be extrapolated to other cardiac walls as there is also a transmural pressure gradient present between ventricle and thorax. However, the exact magnitude of this transmural gradient, and how ventricular/intrathoracic pressure changes within different patient groups should be further studied.

#### V. CONCLUSION

The objective of this work was to find an approach to discriminate a high wave speed as a consequence of elevated LV pressures from a high wave speed as a consequence of elevated myocardial stiffness. Therefore, we used a FEM simulation framework which allowed us to separately study the relevant factors and to investigate the 3D wave propagation patterns and characteristics more in depth. The simulations showed that wave speed gradient might be a valuable tool to distinguish changes in pressure from changes in shear stiffness, which was confirmed in individual human cases. The *in vivo* feasibility of estimating transmural wave speed gradient in different patient groups is under investigation.

#### REFERENCES

- [1] H. Gao, W. Li, L. Cai, C. Berry, and X. Luo, "Parameter estimation in a Holzapfel–Ogden law for healthy myocardium," *Journal of engineering mathematics*, vol. 95, pp. 231-248, 2015.
- [2] H. Kanai, "Visualization of propagation of pulse vibration along the heart wall and imaging of its propagation speed," in *IEEE EMBS Annual International Conference*, New York City, USA, 2006.
- [3] H. J. Vos, B. M. van Dalen, I. Heinenon, J. G. Bosch, O. Sorop, D. J. Duncker, *et al.*, "Cardiac Shear Wave Velocity Detection in the Porcine Heart," *Ultrasound Med Biol*, vol. 43, pp. 753-764, Apr 2017.
- [4] A. P. Sarvazyan, O. V. Rudenko, S. D. Swanson, J. B. Fowlkes, and S. Y. Emelianov, "Shear Wave Elasticity Imaging: a New Ultrasonics Technology of Medical Diagnostics," *Ultrasound Med Biol*, vol. 24, pp. 1419-1435, 1998.
- [5] K. R. Nightingale, M. L. Palmeri, R. W. Nightingale, and G. E. Trahey, "On the feasibility of remote palpation using acoustic radiation force," *J Acoust Soc Am*, vol. 110, pp. 625-634, 2001.
- [6] A. Petrescu, P. Santos, M. Orlowska, J. Pedrosa, S. Bezy, B. Chakraborty, *et al.*, "Velocities of Naturally Occurring Myocardial Shear Waves Increase With Age and in Cardiac Amyloidosis," *JACC Cardiovasc Imaging*, vol. 12, pp. 2389-2398, Dec 2019.
- [7] A. Petrescu, S. Bezy, M. Cvijic, P. Santos, M. Orlowska, J. Duchenne, *et al.*, "Shear Wave Elastography Using High-Frame-Rate Imaging in the Follow-Up of Heart Transplantation Recipients," *JACC Cardiovasc Imaging*, vol. 13, pp. 2304-2313, Nov 2020.
- [8] O. Villemain, M. Correia, E. Mousseaux, J. Baranger, S. Zarka, I. Podetti, *et al.*, "Myocardial Stiffness Evaluation Using Noninvasive Shear Waves Imaging in Healthy and Hypertrophic Cardiomyopathic Adults," *JACC: Cardiovascular Imaging*, vol. 12, pp. 1135-1145, 2018.
- [9] M. Strachinaru, J. G. Bosch, L. van Gils, B. M. van Dalen, A. F. L. Schinkel, A. F. W. van der Steen, *et al.*, "Naturally Occurring Shear Waves in Healthy Volunteers and Hypertrophic Cardiomyopathy Patients," *Ultrasound Med Biol*, vol. 45, pp. 1977-1986, Aug 2019.
- [10] M. Cvijic, S. Bezy, A. Petrescu, P. Santos, M. Orlowska, B. Chakraborty, *et al.*, "Interplay of cardiac remodelling and myocardial stiffness in hypertensive heart disease: a shear wave imaging study using high-frame rate echocardiography," *Eur Heart J Cardiovasc Imaging*, vol. 21, pp. 664-672, Jun 1 2020.
- [11] M. L. Palmeri, K. R. Nightingale, S. Fielding, N. C. Rouze, Y. Deng, L. T., *et al.*, "RSNA QIBA US Shear wave speed phase II phantom study in viscoelastic media," in *IEEE International Ultrasound Symposium*, Taipei, 2015, pp. 1-4.
- [12] N. C. Rouze, M. H. Wang, M. L. Palmeri, and K. R. Nightingale, "Parameters affecting the resolution and accuracy of 2-D quantitative shear wave images," *IEEE Trans Ultrason Ferroelectr Freq Control*, vol. 59, pp. 1729-40, Aug 2012.
- [13] A. Caenen, M. Pernot, D. A. Shcherbakova, L. Mertens, M. Kersemans, P. Segers, *et al.*, "Investigating Shear Wave Physics in a Generic Pediatric Left Ventricular Model via In Vitro Experiments and Finite Element Simulations," *IEEE Trans Ultrason Ferroelectr Freq Control*, vol. 64, pp. 349-361, Feb 2017.
- [14] C. Pislaru, M. W. Urban, S. V. Pislaru, R. R. Kinnick, and J. F. Greenleaf, "Viscoelastic properties of normal and infarcted myocardium measured by a multifrequency shear wave method: comparison with pressure-segment length method," *Ultrasound Med Biol*, vol. 40, pp. 1785-95, Aug 2014.
- [15] S. Bezy, J. Duchenne, M. Orlowska, L. Wouters, A. Caenen, L. B. H. Keijzer, *et al.*, "The behaviour of natural shear waves under different loading conditions," *European Heart Journal*, vol. 41, 2020.
- [16] M. Pernot, M. Couade, P. Mateo, B. Crozatier, R. Fischmeister, and M. Tanter, "Real-time assessment of myocardial contractility using shear wave imaging," *J Am Coll Cardiol*, vol. 58, pp. 65-72, 2011.
- [17] A. E. Werner, S. Bézy, M. Orlowska, J. Duchenne, G. Kubiak, W. Desmet, *et al.*, "Non-invasive assesment of left ventricular filling pressures using cardiac shear wave elastography - a validation study," *Clin Res Cardiol*, vol. 110, p. 1350, Aug 2021.
- [18] P. N. F. Nielsen, L. G. I.J.;, S. B. H.;, and H. P. J.;, "Mathematical model of geometry and fibrous structure of the heart" *Am J Physiol.*, vol. 260, pp. 1365-78, 1991.
- [19] R. M. Lang, L. P. Badano, V. Mor-Avi, J. Afilalo, A. Armstrong, L. Ernande, *et al.*, "Recommendations for cardiac chamber quantification by echocardiography in adults: an update from the American Society of Echocardiography and the European Association of Cardiovascular Imaging," *Eur Heart J Cardiovasc Imaging*, vol. 16, pp. 233-70, Mar 2015.
- [20] D. D. Streeter Jr and W. T. Hanna, "Engineering Mechanics for Successive States in Canine Left Ventricular Myocardium: I. CAVITY AND WALL GEOMETRY," *Circulation Research*, vol. 33, pp. 639-655, 1973.
- [21] G. A. Holzapfel and R. W. Ogden, "Constitutive modelling of passive myocardium: a structurally based framework for material characterization," *Philos Trans A Math Phys Eng Sci*, vol. 367, pp. 3445-75, Sep 13 2009.
- [22] H. Lombaert, J. M. Peyrat, P. Croisille, S. Rapacchi, L. Fanton, F. Cheriet, *et al.*, "Human atlas of the cardiac fiber architecture: study on a

- healthy population," *IEEE Trans Med Imaging*, vol. 31, pp. 1436-47, Jul 2012.
- [23] J. Kocbach, "Finite element modeling of ultrasonic piezoelectric transducers," PhD, Departement of Physics, University of Bergen, Bergen, Norway, 2000.
- [24] A. Caenen, M. Pernot, M. Peirlinck, L. Mertens, A. Swillens, and P. Segers, "An in silico framework to analyze the anisotropic shear wave mechanics in cardiac shear wave elastography," *Physics in medicine and biology*, vol. 63, 2018.
- [25] N. C. Rouze, M. L. Palmeri, and K. R. Nightingale, "Tractable calculation of the Green's tensor for shear wave propagation in an incompressible, transversely isotropic material," *Phys Med Biol*, Nov 27 2019.
- [26] K. Nightingale, "Acoustic Radiation Force Impulse (ARFI) Imaging: a Review," *Curr Med Imaging Rev*, vol. 7, pp. 328-339, Nov 01 2011.
- [27] V. Y. Wang, J. A. Niestrawska, A. J. Wilson, G. B. Sands, A. A. Young, I. J. LeGrice, *et al.*, "Image-driven constitutive modeling of myocardial fibrosis," *International Journal for Computational Methods in Engineering Science and Mechanics*, vol. 17, pp. 211-221, 2016.
- [28] M. W. Urban and J. F. Greenleaf, "Use of the radon transform for estimation of shear wave speed," *The Journal of the Acoustical Society of America*, vol. 132, pp. 1982-1982, 2012.
- [29] A. Ortega, D. Lines, J. Pedrosa, B. Chakraborty, V. Komini, H. Gassert, *et al.*, "HD-PULSE: High channel Density Programmable Ultrasound System based on consumer Electronics," in *IEEE International Ultrasonics Symposium (IUS)*, 2015, pp. 1-3.
- [30] P. Santos, A. Petrescu, J. Pedrosa, M. Orłowska, V. Komini, J.-U. Voigt, *et al.*, "Natural shear wave imaging in the human heart: normal values, feasibility and reproducibility," *IEEE Trans Ultrason Ferroelectr Freq Control*, vol. 66, pp. 442-452, 2018.
- [31] Y. Wang, D. S. Jacobson, and M. W. Urban, "A Non-invasive Method to Estimate the Stress-Strain Curve of Soft Tissue Using Ultrasound Elastography," *Ultrasound Med Biol*, vol. 48, pp. 786-807, May 2022.
- [32] R. Bouchard, D. Hsu, P. Wolf, and G. Trahey, "In Vivo Cardiac Acoustic-Radiation-Force-Driven Shear Wave Velocimetry," *Ultrason Imaging*, vol. 31, pp. 201-213, 2009.
- [33] M. Couade, M. Pernot, E. Messas, A. Bel, M. Ba, A. Hagege, *et al.*, "In vivo quantitative mapping of myocardial stiffening and transmural anisotropy during the cardiac cycle," *IEEE Trans Med Imaging*, vol. 30, pp. 295-305, Feb 2011.
- [34] P. Hollender, D. Bradway, P. Wolf, R. Goswami, and G. Trahey, "Intracardiac acoustic radiation force impulse (ARFI) and shear wave imaging in pigs with focal infarctions," *IEEE Trans Ultrason Ferroelectr Freq Control*, vol. 60, pp. 1669-82, Aug 2013.
- [35] S. Catheline, J. L. Gennisson, and M. Fink, "Measurement of elastic nonlinearity of soft solid with transient elastography," *J Acoust Soc Am*, vol. 114, pp. 3087-91, Dec 2003.
- [36] J. L. Gennisson, M. Renier, S. Catheline, C. Barriere, J. Bercoff, M. Tanter, *et al.*, "Acoustoelasticity in soft solids: assessment of the nonlinear shear modulus with the acoustic radiation force," *J Acoust Soc Am*, vol. 122, pp. 3211-9, Dec 2007.
- [37] S. Aristizabal, C. Amador Carrascal, I. Z. Nenadic, J. F. Greenleaf, and M. W. Urban, "Application of Acoustoelasticity to Evaluate Nonlinear Modulus in Ex Vivo Kidneys," *IEEE Trans Ultrason Ferroelectr Freq Control*, vol. 65, pp. 188-200, Feb 2018.
- [38] M. Bernal, F. Chamming's, M. Couade, J. Bercoff, M. Tanter, and J. L. Gennisson, "In Vivo Quantification of the Nonlinear Shear Modulus in Breast Lesions: Feasibility Study," *IEEE Trans Ultrason Ferroelectr Freq Control*, vol. 63, pp. 101-9, Jan 2016.
- [39] H. Latorre-Ossa, J. L. Gennisson, E. De Brosses, and M. Tanter, "Quantitative imaging of nonlinear shear modulus by combining static elastography and shear wave elastography," *IEEE Trans Ultrason Ferroelectr Freq Control*, vol. 59, pp. 833-9, Apr 2012.
- [40] A. Caenen, M. Pernot, M. Peirlinck, L. Mertens, and P. Segers, "Analyzing the shear wave mechanics in cardiac shear wave elastography using finite element simulations," in *IEEE International Ultrasound Symposium*, Kobe, Japan, 2018.
- [41] A. Caenen, A. Thabit, M. Pernot, D. A. Shcherbakova, L. Mertens, A. Swillens, *et al.*, "The Effect of Stretching on Transmural Shear Wave Anisotropy in Cardiac Shear Wave Elastography," in *IEEE International Ultrasonics Symposium (IUS)*, Washington DC, 2017.
- [42] A. Kolipaka, K. P. McGee, A. Manduca, N. Anavekar, R. L. Ehman, and P. A. Araoz, "In vivo assessment of MR elastography-derived effective end-diastolic myocardial stiffness under different loading conditions," *J Magn Reson Imaging*, vol. 33, pp. 1224-1228, 2011.
- [43] M. W. Urban, B. Qiang, P. Song, I. Z. Nenadic, S. Chen, and J. F. Greenleaf, "Investigation of the effects of myocardial anisotropy for shear wave elastography using impulsive force and harmonic vibration," *Phys Med Biol*, vol. 61, pp. 365-82, 2016.
- [44] O. Pedreira, M. Correia, S. Chatelin, O. Villemain, G. Goudot, S. Thiébaud, *et al.*, "Smart ultrasound device for non invasive real time myocardial stiffness quantification of the human heart," *IEEE Trans Biomed Eng*, 2021.
- [45] W. N. Lee, M. Pernot, M. Couade, E. Messas, P. Bruneval, A. Bel, *et al.*, "Mapping myocardial fiber orientation using echocardiography-based shear wave imaging," *IEEE Trans Med Imaging*, vol. 31, pp. 554-62, 2012.
- [46] H. M. Wang, X. Y. Luo, H. Gao, R. W. Ogden, B. E. Griffith, C. Berry, *et al.*, "A modified Holzapfel-Ogden law for a residually stressed finite strain model of the human left ventricle in diastole," *Biomech Model Mechanobiol*, vol. 13, pp. 99-113, Jan 2014.
- [47] A. Caenen, L. Keijzer, S. Bezy, J. Duchenne, M. Orłowska, A. Van Der Steen, *et al.*, "On the interplay of loading, myocardial stiffness and contractility in transthoracic acoustic radiation force-induced shear wave measurements in pigs," *European Heart Journal-Cardiovascular Imaging*, vol. 23, p. jeab289. 326, 2022.
- [48] J. Bercoff, M. Tanter, M. Muller, and M. Fink, "The Role of Viscosity in the Impulse Diffraction Field of Elastic Waves Induced by the Acoustic Radiation Force," *IEEE Trans Ultrason Ferroelectr Freq Control*, vol. 51, pp. 1523-1536, 2004.
- [49] F. B. C. Cansiz, H. Dal, and M. Kaliske, "An orthotropic viscoelastic material model for passive myocardium: theory and algorithmic treatment," *Computer Methods in Biomechanics and Biomedical Engineering*, vol. 18, pp. 1160-1172, 2015/08/18 2015.
- [50] A. Caenen, D. Shcherbakova, B. Verheghe, C. Papadacci, M. Pernot, P. Segers, *et al.*, "A Versatile and Experimentally Validated Finite Element Model to Assess the Accuracy of Shear Wave Elastography in a Bounded Viscoelastic Medium," *IEEE Trans Ultrason Ferroelectr Freq Control*, vol. 62, pp. 439-450, 2015.